The High Helium Abundance and Charge States of the Interplanetary CME and Its Material Source on the Sun

Hui Fu[1,2] , R. A. Harrison[2], J. A. Davies[2], LiDong Xia[1] , XiaoShuai Zhu[3] , Bo Li[1] , ZhengHua Huang[1] , and D. Barnes[2]

[1] Shandong Key Laboratory of Optical Astronomy and Solar-Terrestrial Environment, Institute of Space Sciences, Shandong University, Weihai, Shandong, 264209, People's Republic of China; fuhui@sdu.edu.cn

[2] STFC-RAL Space, Rutherford Appleton Laboratory, Harwell Campus, Didcot, OX11 0QX, UK

[3] Max Planck Institute for Solar System Research, Justus-von-Liebig-Weg 3, D-37077, Göttingen, Germany

Abstract

Identifying the source of the material within coronal mass ejections (CMEs) and understanding CME onset mechanisms are fundamental issues in solar and space physics. Parameters relating to plasma composition, such as charge states and He abundance (A_{He}), may be different for plasmas originating from differing processes or regions on the Sun. Thus, it is crucial to examine the relationship between in situ measurements of CME composition and activity on the Sun. We study the CME that erupted on 2014 September 10, in association with an X1.6 flare, by analyzing Atmospheric Imaging Assembly imaging and Interface Region Imaging Spectrograph (IRIS) spectroscopic observations and its in situ signatures detected by Wind and Advanced Composition Explorer. We find that during the slow expansion and intensity increase of the sigmoid, plasma temperatures of 9 MK, and higher, first appear at the footpoints of the sigmoid, associated with chromospheric brightening. Then the high-temperature region extends along the sigmoid. IRIS observations confirm that this extension is caused by transportation of hot plasma upflow. Our results show that chromospheric material can be heated to 9 MK, and above, by chromospheric evaporation at the sigmoid footpoints before flare onset. The heated chromospheric material can transport into the sigmoidal structure and supply mass to the CME. The aforementioned CME mass supply scenario provides a reasonable explanation for the detection of high charge states and elevated A_{He} in the associated interplanetary CME. The observations also demonstrate that the quasi-steady evolution in the precursor phase is dominated by magnetic reconnection between the rising flux rope and the overlying magnetic field structure.

Unified Astronomy Thesaurus concepts: Solar-terrestrial interactions (1473); Solar corona (1483); Solar coronal mass ejections (310); Solar flares (1496); Solar abundances (1474)

1. Introduction

The Earth is in coronal mass ejection (CME) outflow for ∼10% of the time at solar minimum up to 35% at solar maximum (Cliver et al. 2003). Therefore, the CME generation mechanism and the source of CME material are important issues in heliophysics.

Studies of the relationship between in situ parameters, such as charge states, helium (He) abundance (A_{He}), first ionization potential (FIP) bias, and activity in the source region can promote understanding of mass supply to CMEs and the connection between CMEs and flares. These composition parameters carry information from the near-Sun region where CMEs are forming, the solar wind is accelerating, and the corona is heated (e.g., Manchester et al. 2017). Beyond several solar radii, the ion charge state, such as the number density ratio of O^{7+} to O^{6+} (O^{7+}/O^{6+}), is "frozen in." Therefore, the charge states farther from the Sun represent the temperature of the coronal source region (Lepri et al. 2001). The average iron (Fe) charge state (Q_{Fe}) is 9^+ to 11^+ in the solar wind (Lepri et al. 2001). In contrast, more than 90% of long-duration higher-Q_{Fe} episodes (greater than 12 for more than 6 hr) occur inside interplanetary CMEs (ICMEs) and around half of the ICMEs are accompanied by high Q_{Fe} (Lepri et al. 2001; Lepri & Zurbuchen 2004). Low FIP elements, such as Mg, Si, and Fe, are usually more abundant in the solar wind and corona than in the photosphere (the FIP bias effect; Feldman 1992). Conversely, the high FIP element helium is usually less abundant in the corona and solar wind than in the photosphere. A possible explanation for the enrichment of low FIP elements (i.e., FIP bias effect) and depletion of helium in the corona/solar wind is that the mechanism that transports the element to the upper atmosphere is only valid to ions (Laming 2015).

Statistically, the charge states, A_{He}, and the FIP bias inside ICMEs are higher than in the background solar wind (Richardson & Cane 2004; Manchester et al. 2017; Owens 2018). However, the variation in these parameters over a single ICME, and between different ICMEs, can be so significant that they cannot be used for definitive ICME identification (Richardson & Cane 2004). In some ICMEs, the source temperatures that are deduced from the charge states can exceed 10 MK, which can only be achieved by heating by flares (Gopalswamy 2006). Statistical results show that Q_{Fe} and O^{7+}/O^{6+} in an ICME correlate positively, but only weakly, with flare class (Reinard 2008; Gopalswamy et al. 2013). This suggests that plasma that has been heated by flares is not always a source of CME material. Borrini et al. (1982) found that ICMEs associated with strong flares, on average, have higher A_{He}, although Reinard (2008) found no clear correlation between A_{He} in an ICME and flare intensity. The reason for elevated A_{He} in ICMEs is not clear (Manchester et al. 2017).

If flare-heated plasma is injected into CMEs, then the accompanying ICMEs should have higher charge states. Plasma can be heated to a temperature of 10 MK and higher by two processes during flares: (1) magnetic reconnection in the corona (Lin et al. 2005; Su et al. 2013) and (2)

chromospheric evaporation (Tian et al. 2013, 2015; Young et al. 2013). In the latter, electrons are energized by magnetic reconnection in the corona, and then propagate downwards where they heat the chromosphere via Coulomb collisions.

Generally, it is believed that the hot plasma inside ICMEs can be heated directly by magnetic reconnection between the flux rope and flare loops during the flaring process (Priest & Forbes 2002; SONG et al. 2015; Song et al. 2016). It is not known if the heated chromosphere can supply mass to CMEs. $A_{\rm He}$ may not be the same for the two different hot plasma sources. $A_{\rm He}$ in a CME should be lower than in the photosphere if the plasma is heated by magnetic reconnection directly in the corona, as $A_{\rm He}$ is lower in the corona compared with that in the photosphere (Laming 2015, and references therein). In contrast, $A_{\rm He}$ in plasma heated by chromospheric evaporation may be the same as in the photosphere (i.e., higher than in corona) if the helium is still neutral prior to being heated.

Using the 2014 September 10 CME as a case study, we address the question of why $A_{\rm He}$ can be nearly as high as in the photosphere in some ICMEs, and where that material originates. In the present study, we analyze (1) the morphology evolution of a hot channel, (2) chromospheric brightening and plasma heating at the sigmoidal footpoints, (3) transportation of hot plasma along the sigmoid, and (4) the connection between the aforementioned phenomena during the precursor phase of the flare (corresponding to the CME initiation phase). The in situ parameters relating to composition are also analyzed.

2. Instruments and Data Analysis

An X1.6 flare took place in NOAA Active Region (AR) 12158, with the peak of the Geostationary Operational Environmental Satellite (GOES) soft X-ray (SXR) intensity occurring at about 17:45 UT on 2014 September 10. The remote-sensing data used to study the solar atmosphere during this event are mainly from the Atmospheric Imaging Assembly (AIA; Lemen et al. 2012) and the Helioseismic and Magnetic Imager (HMI; Schou et al. 2012) on board the Solar Dynamics Observatory (SDO; Pesnell et al. 2012), and the Interface Region Imaging Spectrograph (IRIS; De Pontieu et al. 2014). AIA images the solar atmosphere in seven EUV passbands and three UV passbands ranging in temperature from $6 \times 10^4 K$ to $2 \times 10^7 K$. The spatial resolution of AIA is 1.2 arcsec and the temporal resolution is 12 s and 24 s for EUV and UV passbands, respectively. HMI provides measurements of the vector magnetic field in the photosphere. IRIS can obtain spectral data and slit-jaw images simultaneously. For the former, the spatial resolution is 0.166 arcsec per pixel, and the cadence is 9.5 s. IRIS observations were taken between 11:28 and 17:59 UT on 2014 September 10 in a sit-and-stare mode. The IRIS slit crossed the main part of a hot channel near its east footpoint. The formation temperature of the Fe XXI 1354.08 Å line is about 11 MK (Landi et al. 2013). This is the only IRIS line that is formed at a temperature higher than 2 MK (Tian et al. 2015). Here, we use this line to examine the transport of hot plasma associated with the hot channel.

To analyze the heating and plasma transportation in more detail, we calculate the differential emission measure (DEM) using improved tools developed by Cheung et al. (2015) and Su et al. (2018). We reconstruct the 3D magnetic field structures of the active region using the HMI vector magnetograms using the method of Zhu et al. (2013, 2016).

The speed of the associated CME was very high; the linear speed is ~ 1267 km s^{-1} near the Sun (based on the CDAW catalog[4]). This event is also identified in the HELCATS[5] catalog of CMEs observed in Solar TErrestrial RElations Observatory (STEREO) heliographic imager data. The radial speed of the CME derived from geometrical fitting to its time-elongation profile (Davies et al. 2013) is ~ 1000 km s^{-1}. The CDAW and HELCATS catalogs suggest a transit time to Earth of 2 days. Consistent with this prediction, a CME is detected by the Wind[6] (Acuña et al. 1995) and Advanced Composition Explorer (ACE[7]; Stone et al. 1998) spacecraft near the Earth during the latter half of 2014 September 12. This is the only CME detected near the Earth within several days of this predicted arrival time.

The velocities and number densities of the proton and helium ions of the CME were measured by the Solar Wind Experiment (SWE) Faraday cup instruments (Ogilvie et al. 1995) on board Wind. $A_{\rm He}$, expressed as a percentage, is derived from the ratio of the number density of helium ions to protons. The ICME magnetic field was recorded by the Wind Magnetic Field Investigation (MFI; Lepping et al. 1995). The average charge state of $Q_{\rm Fe}$ and the O^{7+}/O^{6+} ratio were based on measurements from the Solar Wind Ion Composition Spectrometer (SWICS; Gloeckler et al. 1998) on board ACE.

3. Observational Results

3.1. The Morphology Evolution and Brightness Variation before the Flare Onset

Figure 1 shows the morphology evolution and the footpoint brightenings of the hot channel. The images display a well-developed active region (AR 12158) with a large sigmoidal-shaped channel identified in the hot EUV-emitting plasma. The sigmoidal structure on AIA 131 Å images existed for ~ 1 hr before CME eruption, and is already well formed by $\sim 17:00$ UT (Figure 1(b)). The hot channel (sigmoid) is believed to represent a magnetic flux rope (MFR; Zhang et al. 2012; Liu et al. 2018), which should be mature by this time. From 17:00 UT, the sigmoid structure in AIA 131 Å images (formation temperature ~ 10 MK) becomes increasingly bright, and enlarges.

During the slow expansion and intensity increase of the sigmoid before the flare onset (17:22 UT), chromospheric brightening occurs at the footpoints of the sigmoid (brightenings inside blue and brown big rectangles in Figure 1 (c)); the intensity of those footpoint regions also increase in 131 Å. The chromosphere intensity variations of the footpoint regions are shown in Figure 1(d) for clarity but will be discussed in Section 3.3. These observations demonstrate that the brightening and expansion of the sigmoid may be closely related to the brightening of its chromospheric footpoints.

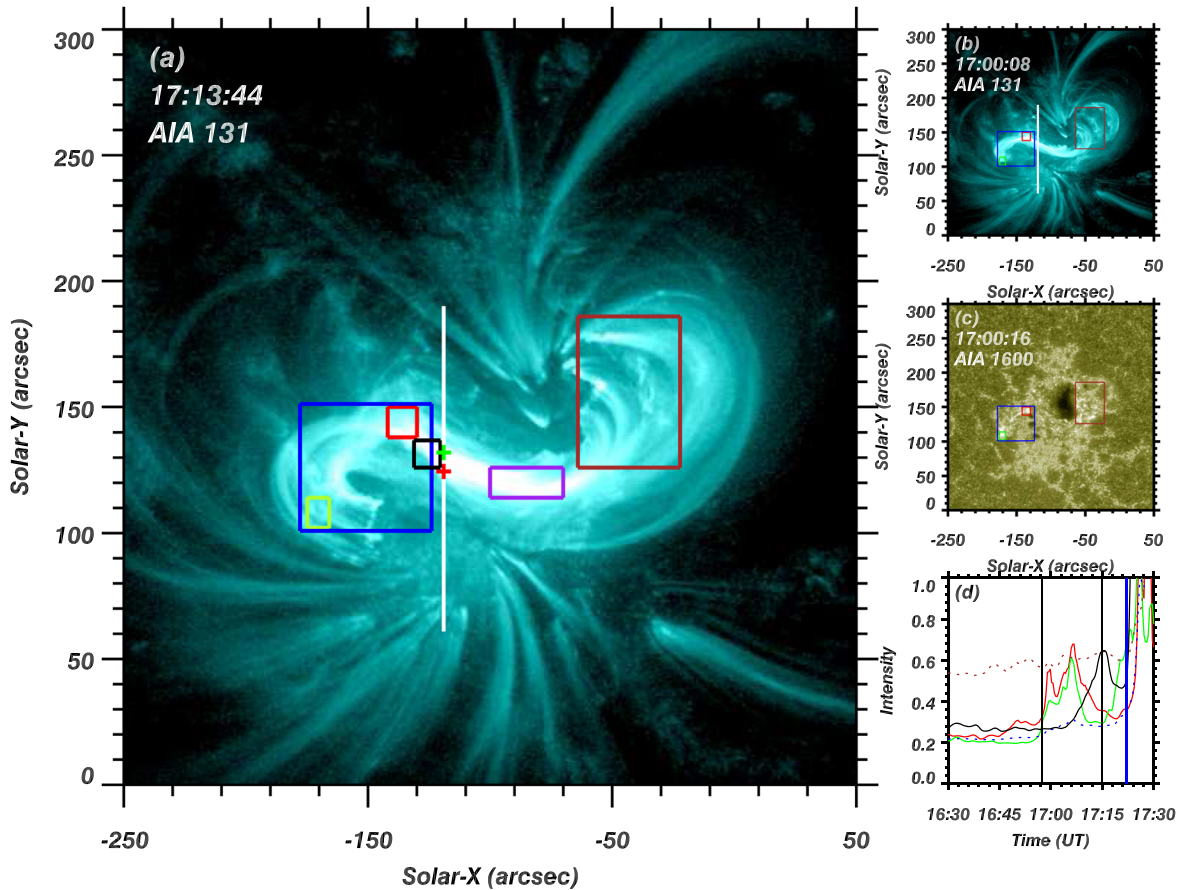### 3.2. The Temperature Evolution at the Footpoints and in the Main Body of the Hot Channel

The DEM in the center part (purple rectangle in Figure 1(a)) of the hot channel is shown in Figure 2(a). The peak of the distribution is located at ~ 8 MK, which demonstrates the high

---

4   https://cdaw.gsfc.nasa.gov/CME_list/
5   https://www.helcats-fp7.eu/index.html
6   https://cdaweb.gsfc.nasa.gov/index.html
7   http://www.srl.caltech.edu/ACE

Figure 1. Morphology evolution and the footpoint brightenings of the hot channel. The evolution of the sigmoidal structure in the higher-temperature AIA images (131 Å) is shown in panels (a) and (b), and the chromospheric brightening (AIA 1600 Å) is shown in (c). The chromosphere intensity variations of the footpoint regions are shown in (d). The white vertical lines in (a) and (b) represent the location of the IRIS slit, and the green and red plus signs that lie on that line denote the north and south loops that are intense in the IRIS Fe XXI spectrum. The purple rectangle represents the center part of the hot channel, and the other large and small rectangles denote the footpoints of the sigmoidal structure.

temperature of the hot channel. During the evolution, the peak of the distribution increased significantly, indicating an increase in the amount of hot plasma inside the hot channel.

Emission measure (EM) images with temperature between 9 and 20 MK are shown in Figures 2(b) and (c). High-temperature plasma first appears at the left (eastern) sigmoid footpoint (red rectangle) at 16:58:08 UT, and then extends along the length of the sigmoid. We choose six rectangles along the sigmoidal structure from its left footpoint to the far right (see Figures 2(b) and (c)). The temporal variations of the average EM (9–20 MK) in these six boxes are shown in Figures 2((d1)–(d3)), in the same colors as the boxes. The average EM for all six subregions is significantly lower than 27 before 16:58 UT showing that the plasma temperature is lower than 9 MK. The variation of the EM (9–20 MK), averaged in the footpoint region (green line in Figure 2(d1)), mirrors the intensity increase and decrease in the chromospheric images (red line in Figure 2(d1)). The chromospheric brightening in the footpoint region and the EM (9–20 MK) both start to increase at 16:58 UT before reducing at about 17:14 UT. The synchronization of these two phenomena in this footpoint region means that the plasma was heated to values above 9 MK with the brightening in the chromosphere.

Plasma hotter than 9 MK first appears in the leftmost rectangle (Figure 2(d1)) at 16:58 UT and in the rightmost rectangle, 50 arcsec away by 17:08 UT (d3). Therefore, the hot

plasma extends along the sigmoidal structure at a speed of ∼60 km s^{-1}. But does this speed represent the actual flow of the hot material or not?

3.3. The Blueshift of Fe XXI 1354 Å Observed by IRIS

The IRIS slit (white vertical line in Figures 1 and 2) was over the main part of the sigmoid near its eastern footpoint. IRIS Fe XXI 1354.08 Å spectra taken at different times are shown in Figures 3(a1)–(a3); Figures 3(b1)–(b3) present spectra from Si IV 1402.82 Å. The C I 1354.288 Å lies close to the Fe XXI 1354.08 Å in the spectrum, but is much narrower as it emitted from neutral atoms and its Doppler shift is nearly zero (Tian et al. 2015). Therefore, we use this line to calibrate the Fe XXI 1354.08 Å.

The Fe XXI 1354.08 Å spectrum is intense near solar y = 135 and 125 arcsec. These positions are delimited by pairs of horizontal yellow and golden lines in Figure 3, respectively, and marked by the two plus signs in Figure 1(a). The Fe XXI line intensity starts to increase at 17:01 UT at 135 arcsec; later, from about 17:11 UT, the intensity in the south part of the slit starts to increase. In both locations, the Fe XXI line is blueshifted, and the Doppler speed of the north (south) loop is about 10–20 (100) km s^{-1}. This demonstrates that higher-temperature plasma propagates from lower to higher altitudes in the north and south loops systems.
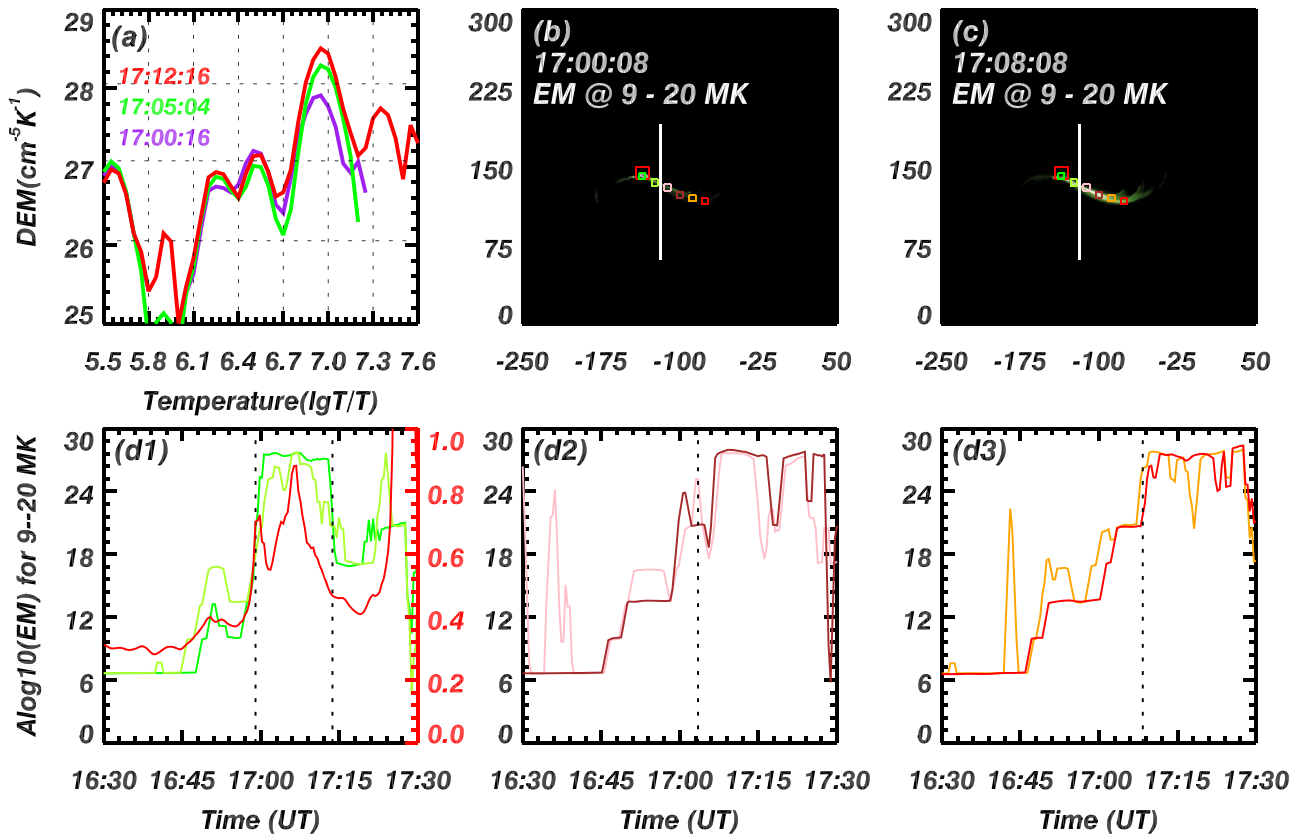
Figure 2. The DEM of the hot channel. The DEM for the center part of the hot channel is shown in (a). The evolution of the EM in the temperature rang from 9 to 20 MK is shown in (b) and (c). The six colored rectangles span the sigmoidal structure from the left footpoint to the far right, and the white vertical lines show the location of the IRIS slit. The variation of the average EM (9–20 MK) for the six boxes is shown in the bottom panels, in corresponding colors. The chromospheric intensity variations for the footpoint are shown in (d1) with red.

We believe that the hot plasma flows in both north and south loops come from the footpoint regions represented by red and black boxes in Figure 1(a). First, the high-temperature plasma first appears at the sigmoid footpoint and then extends along the sigmoidal structure (Figures 2(b) and (c)). Second, the time ranges over which the Fe XXI 1354.08 Å line is blueshifted in the north (16:58–17:13 UT) and south (17:12–17:18 UT) loop systems coincide with the brightening due to plasma heating in the red and black boxes (Figure 1(d)), respectively.

Furthermore, we examine the chromospheric lines at the location where the Fe XXI 1354.08 Å line is intense and blueshifted. The results confirm those of Cheng & Ding (2016), in that the chromospheric lines do not brighten, broaden, or shift between 17:01 UT and 17:14 UT (see Figures 3 (b1) and (b2)), meaning that the hot plasma upflow is not generated in the low atmosphere where the IRIS slit is located.

Therefore, the spectroscopic observations confirm that the higher-temperature plasma generated at sigmoid footpoints can propagate along with the sigmoid structure (with ∼100 km s^{-1} speed) and, moreover, supply mass to the CME due to the fact that the sigmoid (hot channel) represents the helical MFR (Zhang et al. 2012; Liu et al. 2018).

We believe that the plasma at the sigmoid footpoints is heated by chromospheric evaporation, not by magnetic reconnection at the footpoint directly, for the following reasons:

First, the average intensities of the right and left footpoint regions (blue and brown dotted rectangles in Figure 1(a) and dotted lines in Figure 1(d)) are both increasing gradually during the slow expansion of the sigmoid. The brightening in different subregions of the same footpoint (green and red small rectangles in Figure 1(a) and lines in Figure 1(d)) even occur near-simultaneously. This is hard to explain by magnetic reconnection. Second, direct evidence for chromospheric evaporation is provided by spectroscopic observations taken after 17:14:30 UT. When the area of chromospheric brightening extends to the IRIS slit, the intensities of the Fe XXI 1354.08 Å and Si IV 1402.82 Å lines are increased in the southern loop system. The former is strongly blueshifted, and the latter is brightened, broadened, and redshifted (Figures 3(a3) and (b3)). The scenario is the same as for the standard chromospheric evaporation process, except that the rate of evaporation is weaker than for the impulsive phase of the flare.

3.4. The Overall Magnetic Field Structure of the Active Region

To explore where and how the higher-energy nonthermal electrons are generated, we show the magnetic field structures of the active region in Figure 4(a). The sigmoid is clearly covered by overlying magnetic field structures. The scenario of the whole process is illustrated in Figure 4(c). High-energy, nonthermal electrons, produced by magnetic reconnection between the rising flux rope and the overlying magnetic field structure (step 1 in Figure 4(c)), are transported downwards to the sigmoid footpoints (step 2). These nonthermal electrons then cause heating of the chromospheric material (step 3). The heated chromospheric material is then transported upwards into the sigmoidal structure along the magnetic field lines (step 4).
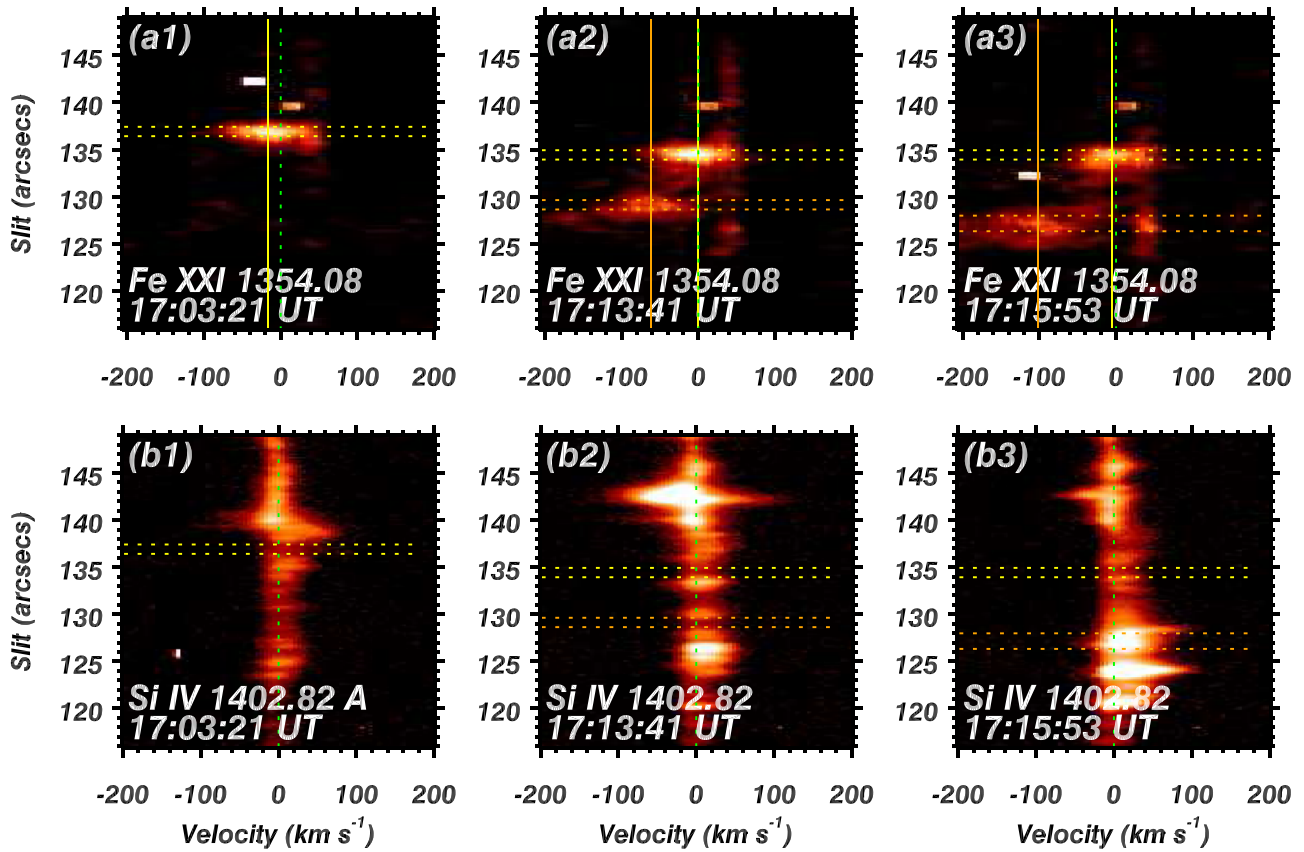
Figure 3. The IRIS spectroscopy observations. Fe XXI 1354.08 Å and Si IV 1402.82 Å spectra are shown in the top and bottom rows, respectively. The green dotted lines represent the location where the Doppler shift of the Fe XXI 1354.08 Å line is zero. The intensity of the regions between the pairs of yellow and golden horizontal lines in the Fe XXI 1354.08 Å spectrum is higher than elsewhere, and the line centers were deduced from measurements in those regions. The yellow and golden solid vertical lines in the top panels denote the deduced line centers for Fe XXI 1354.08 Å for northern and southern loop systems, respectively.
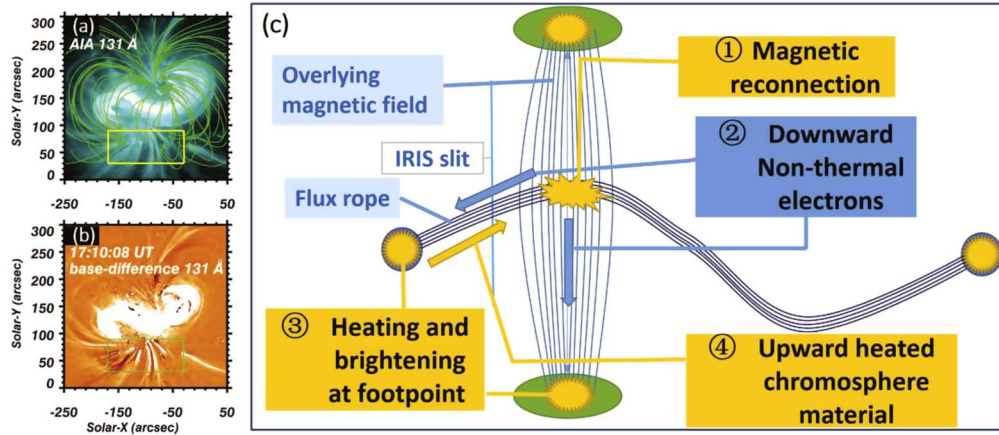
Figure 4. The overall magnetic field structure of the active region is shown in (a). Base-difference 131 Å image is shown in (b). Rectangles enclose the footpoint region of the overlying magnetic field structure. The scenario for magnetic reconnection between the rising flux rope and the overlying magnetic field structure, downward nonthermal electrons, chromospheric evaporation at the footpoint, and upflowing heated plasma are shown in (c).

The observed phenomena, such as the time correspondence of footpoint brightening, heating in the footpoint regions, and high-temperature plasma upflow, along with the presence of the sigmoidal structure, are all consistent with the picture.

In this scenario, the intensity of the footpoints of the overlying magnetic field structure should also increase (Yang et al. 2019). A base-difference 131 Å image is presented in Figure 4(b). Note that the intensity of the overlying magnetic

field structure footpoint region (green rectangles) was also enhanced. This supports the scenario illustrated in Figure 4(c).

3.5. The In Situ Properties of the ICME

Figure 5 shows the in situ parameters of the associated ICME from Wind and ACE. There is a high-density sheath in front of the magnetic cloud (MC), because the ICME speed (600 km s^{-1}) was much higher than the background solar wind (400 km s^{-1}). Note that the charge states and A_{He} in the sheath
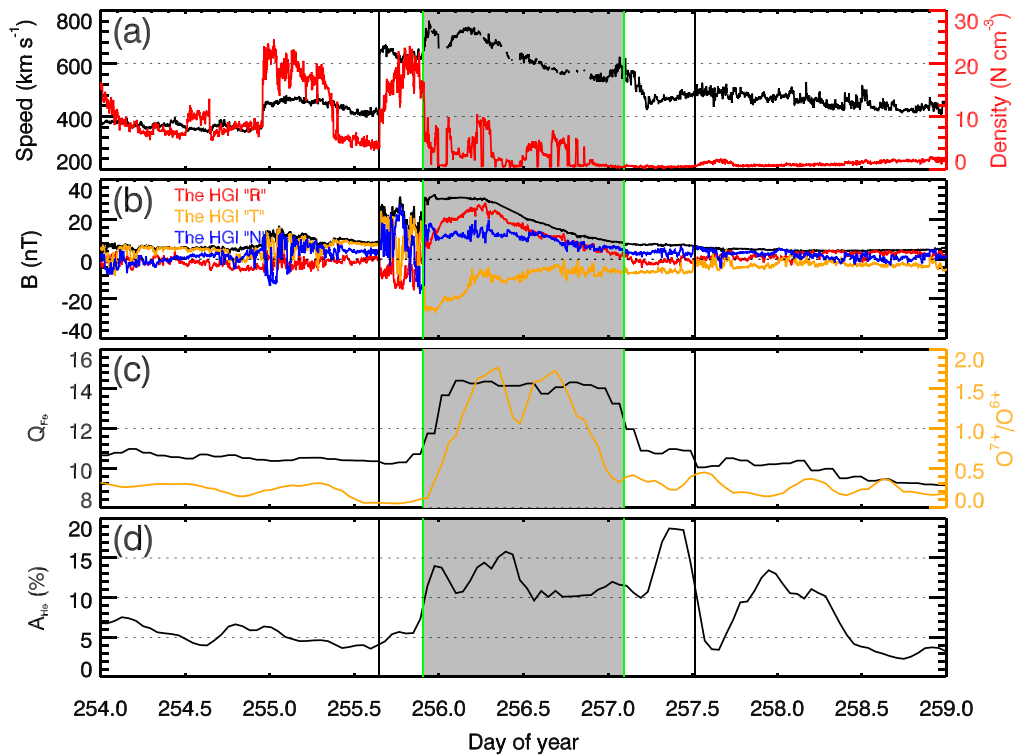
Figure 5. The in situ parameters of the ICME and the background solar wind. The speed and density are shown in (a), magnetic field in (b), average charge state of Fe and density ratio of O^{7+} and O^{6+} in (c), and helium abundance in (d). The two black vertical lines represent the start and end of the ICME passage, and the MC is represented by the gray region bounded by green vertical lines. The charge state of Q_{Fe} and the O^{7+}/O^{6+} are much higher inside the MC than elsewhere in the ICME/ in the solar wind, and the A_{He} is also as high as it is in the photosphere.

are not elevated; they are almost the same as in the upstream solar wind, indicating that the sheath is composed of swept-up material. The average Q_{Fe} (O^{7+}/O^{6+}) reaches 15 (1.5) inside the MC, but is only $\sim$10 (0.2) in the surrounding background solar wind, indicating that the source temperature of the ICME is much higher than that of the background solar wind. Interestingly, A_{He} inside the MC is $\sim$10–15%, which is even higher than the average A_{He} in the photosphere.

4. Discussion

4.1. Why is the Helium Abundance so High in ICMEs?

It is not known why A_{He} is so high in some ICMEs (Neugebauer & Goldstein 1997; Manchester et al. 2017). Neugebauer & Goldstein (1997) speculated that a "sludge removal phenomenon" transports lower atmosphere material with higher A_{He} into the heliosphere together with the CMEs. Here, we find that chromosphere material heated by chromospheric evaporation at the footpoints can be transported into the sigmoidal structure before flare onset. It is believed that the sigmoid represents the helical MFR (Zhang et al. 2012; Liu et al. 2018) and corresponds to the MC inside ICME. Therefore, in our case, the hot plasma inside the ICME comes from the chromosphere before flare onset. The timescale for the FIP bias effect is several days (Baker et al. 2013), whereas chromospheric evaporation is much faster. If He (ionization temperature $\sim$50,000K) is still neutral in the chromosphere prior to being heated, the A_{He} of the heated plasma should also be high, equal even, to its value in the photosphere. The aforementioned scenario for the mass supply of the CME can explain the high A_{He} and charge states inside ICMEs.

4.2. The Connection between the Evolution Pre- and Post-flare Onset

Zhang et al. (2001) speculated that the development of the physical process that occurs before the flare onset is what results in the eruption of CMEs and flares. Here, we present a more detailed picture of the connection between flares and CMEs in the precursor phase (as shown in Figure 4(c)). Magnetic reconnection between the flux rope and the overlying loops is triggered by the rising of the flux rope. Nonthermal electrons produced by the magnetic reconnection cause heating of the chromospheric material, which is then transported upwards into the sigmoidal structure. The sigmoid brightens and further expands. This expansion increases the rate of magnetic reconnection. Chromospheric evaporation that occurs at the footpoint and the magnetic field reconnection that occurs at higher altitudes exacerbate each other. This system evolves much faster after the onset of the flare, and the standard CME and flare model should be valid during the impulsive phase. Our findings demonstrate that evolution before flare onset is crucial for the eruption of the flare and CME. Flares and CMEs have a close relationship, and they are different manifestations of the same active magnetic field system (Harrison 1995, 2003).

5. Conclusion

We have examined the relationship between the in situ parameters of the ICME and activity on the Sun. In the source region, we focus on the connection between sigmoid evolution and chromospheric brightening at the sigmoid footpoints before flare onset. We find that:

1. During the slow expansion and intensity increase of the sigmoid, the high-temperature plasma first appears at the footpoints of the sigmoid, associated with chromospheric brightening. Then the high-temperature region extends along the sigmoid.
2. The spectroscopic observations demonstrate that the extension of the higher-temperature structure is caused by the upflowing hot plasma and the material at the sigmoid footpoints are heated by chromospheric evaporation.

Our results demonstrate that chromosphere material can be heated to higher than 9 MK by chromospheric evaporation at the sigmoid footpoints before flare onset. The heated chromospheric material can be transported into the sigmoidal structure and supply mass to the CME. This mass supply scenario provides a reasonable explanation for the high charge states and elevated A_{He} of the associated ICME.

ORCID iDs

Hui Fu ⓘ https://orcid.org/0000-0002-8827-9311
LiDong Xia ⓘ https://orcid.org/0000-0001-8938-1038
XiaoShuai Zhu ⓘ https://orcid.org/0000-0002-1682-1714
Bo Li ⓘ https://orcid.org/0000-0003-4790-6718
ZhengHua Huang ⓘ https://orcid.org/0000-0002-2358-5377
D. Barnes ⓘ https://orcid.org/0000-0003-1137-8220

References

Acuña, M. H., Ogilvie, K. W., Baker, D. N., et al. 1995, SSRv, 71, 5
Baker, D., Brooks, D. H., Démoulin, P., et al. 2013, ApJ, 778, 69
Borrini, G., Gosling, J. T., Bame, S. J., & Feldman, W. C. 1982, JGR, 87, 7370
Cheng, X., & Ding, M. D. 2016, ApJL, 823, L4
Cheung, M. C. M., Boerner, P., Schrijver, C. J., et al. 2015, ApJ, 807, 143
Cliver, E. W., Ling, A. G., & Richardson, I. G. 2003, ApJ, 592, 574
Davies, J. A., Perry, C. H., Trines, R. M. G. M., et al. 2013, ApJ, 777, 167
De Pontieu, B., Title, A. M., Lemen, J. R., et al. 2014, SoPh, 289, 2733
Feldman, U. 1992, PhyS, 46, 202
Gloeckler, G., Cain, J., Ipavich, F. M., et al. 1998, SSRv, 86, 497
Gopalswamy, N. 2006, SSRv, 124, 145
Gopalswamy, N., Mäkelä, P., Akiyama, S., et al. 2013, SoPh, 284, 17
Harrison, R. A. 1995, A&A, 304, 585
Harrison, R. A. 2003, AdSpR, 32, 2425
Laming, J. M. 2015, LRSP, 12, 2
Landi, E., Young, P. R., Dere, K. P., Del Zanna, G., & Mason, H. E. 2013, ApJ, 763, 86
Lemen, J. R., Title, A. M., Akin, D. J., et al. 2012, SoPh, 275, 17
Lepping, R. P., Acūna, M. H., Burlaga, L. F., et al. 1995, SSRv, 71, 207
Lepri, S. T., & Zurbuchen, T. H. 2004, JGRA, 109, A01112
Lepri, S. T., Zurbuchen, T. H., Fisk, L. A., et al. 2001, JGR, 106, 29231
Lin, J., Ko, Y. K., Sui, L., et al. 2005, ApJ, 622, 1251
Liu, T., Su, Y., Cheng, X., van Ballegooijen, A., & Ji, H. 2018, ApJ, 868, 59
Manchester, W., Kilpua, E. K. J., Liu, Y. D., et al. 2017, SSRv, 212, 1159
Neugebauer, M., & Goldstein, R. 1997, GMS, 99, 245
Ogilvie, K. W., Chornay, D. J., Fritzenreiter, R. J., et al. 1995, SSRv, 71, 55
Owens, M. J. 2018, SoPh, 293, 122
Pesnell, W. D., Thompson, B. J., & Chamberlin, P. C. 2012, SoPh, 275, 3
Priest, E. R., & Forbes, T. G. 2002, A&ARv, 10, 313
Reinard, A. A. 2008, ApJ, 682, 1289
Richardson, I. G., & Cane, H. V. 2004, JGRA, 109, A09104
Schou, J., Scherrer, P. H., Bush, R. I., et al. 2012, SoPh, 275, 229
SONG, H. Q., CHEN, Y., ZHANG, J., et al. 2015, ApJL, 808, L15
Song, H. Q., Zhong, Z., Chen, Y., et al. 2016, ApJS, 224, 27
Stone, E. C., Frandsen, A. M., Mewaldt, R. A., et al. 1998, SSRv, 86, 1
Su, Y., Veronig, A. M., Hannah, I. G., et al. 2018, ApJL, 856, L17
Su, Y., Veronig, A. M., Holman, G. D., et al. 2013, NatPh, 9, 489
Tian, H., Tomczyk, S., McIntosh, S. W., et al. 2013, SoPh, 288, 637
Tian, H., Young, P. R., Reeves, K. K., et al. 2015, ApJ, 811, 139
Yang, S., Zhang, J., Song, Q., Bi, Y., & Li, T. 2019, ApJ, 878, 38
Young, P. R., Doschek, G. A., Warren, H. P., & Hara, H. 2013, ApJ, 766, 127
Zhang, J., Cheng, X., & Ding, M.-D. 2012, NatCo, 3, 747
Zhang, J., Dere, K. P., Howard, R. A., Kundu, M. R., & White, S. M. 2001, ApJ, 559, 452
Zhu, X., Wang, H., Du, Z., & He, H. 2016, ApJ, 826, 51
Zhu, X. S., Wang, H. N., Du, Z. L., & Fan, Y. L. 2013, ApJ, 768, 119